Assessment of suspended sediment concentration at the Hangzhou Bay using HJ CCD imagery

LIU Wangbing[1], YU Zhifeng[2,3], ZHOU Bin[2], JIANG Jingang[2], PAN Yuliang[2], LING Zaiying[2]

1. *Institute of Applied Remote Sensing and Information Technology, Zhejiang University, Hangzhou* 310058, *China*;
2. *Institute of Remote Sensing and Earth Sciences, Hangzhou Normal University, Hangzhou* 311121, *China*;
3. *State Key Laboratory of Information Engineering in Surveying, Mapping and Remote Sensing Wuhan University, Wuhan* 430079, *China*

Abstract: This research explored the potential of the use of the CCD image of the HJ satellite to derive Suspended Sediment Concentrations (SSC) of dynamic water bodies at Hangzhou Bay, which is a typical turbid water body in China. Through the analysis on the correlation between Remote Sensing Reflectance (R_{rs}) and SSC, two apparent reflectance peaks at approximately 690 and 830 nm have been found in the third and fourth bands, respectively. The result also shows that a good correlation exists between R_{rs} and SSC when the wavelength is more than 700 nm. Based on the measured correlation between SSC and R_{rs}, the retrieval model is established using the ratio of band4 and band3 as remote sensing factor, and the model determination coefficient of 0.90 is reached. Through the Moderate Resolution Imaging Spectroradiometer (MODIS)-derived Aerosol Optical Depth (AOD) data, which are calculated from the Near Infrared-Short Wave Infrared (NIR-SWIR) atmospheric correction, the atmospheric correction of HJ CCD imagery is realized. The correction-relative errors of the third and fourth bands are 5.54% and 6.97%, respectively. The result demonstrates that the relative error of SSC derived from HJ CCD imagery is 7.12%, and SSC at Hangzhou Bay, which also has significant internal diversity, is much higher than that in the entrance of the Yangtze River. This research demonstrated that HJ CCD imagery can be used to evaluate SSC at Hangzhou Bay, if the appropriate atmospheric correction method and retrieval algorithm are used.

Key words: HJ CCD, Hangzhou Bay, SSC, remote sensing reflectance, atmospheric correction

CLC number: TP79 **Document code:** A

Citation format: **Liu W B, Yu Z F, Zhou B, Jiang J G, Pan Y L and Ling Z Y. 2013. Assessment of suspended sediment concentration at the Hangzhou Bay using HJ CCD imagery. Journal of Remote Sensing, 17(4): 905-918 [DOI: 10.11834/jrs.20132195]**

1 INTRODUCTION

Case Ⅱ waters, which are distributed mainly in coastal and estuarine areas, are presently polluted by land materials (Morel & Prieur, 1977). With the rapid economic development, water pollution along the shorelines and in the coastal areas is highly increasing. Suspended sediments, as one of the biogeochemical "core parameters", are important in defining spectral characteristics of case Ⅱ waters. The quantity level of suspended sediment concentration not only directly affects optical properties (e.g., transparency, turbidity, color), but also changes the processes of aquatic conditions, erosion, and deposition in the channels and in coastal areas (Cheng & Zhao, 1985). In addition, pollutants carried by suspended sediments significantly affect water quality of coastal and inland waters (Tassan, 1997). Regular field measurement and sampling, as traditional methods of water quality monitoring, however, are not only money and time consuming, but can also only obtain limited data that cannot support the monitoring of spatio-temporal changes in a large region. Therefore, a new way to provide bio-optical observation of long-term indicators for water quality monitoring is needed.

With its unique spatio-temporal advantages, remote sensing has become an effective tool for dynamic monitoring of water quality in large areas (Gin, et al., 2003). Present marine color sensors, such as the Coastal Zone Color Scanner (CZCS), Sea-viewing Wide Field-of-view Sensor (SeaWiFS), Medium Resolution Imaging Spectrometer (MERIS), and Moderate Resolution Imaging Spectroradiometer (MODIS), as well as land s

Received: 2012-06-27; **Accepted:** 2012-10-23; **Version of record first published:** 2012-10-30

Foundation: National Natural Science Foundation of China (No. 40971193, 41206169, 41206168); The Marine Public Welfare Industries Earmarked Fund (No. 200905012, 201005030); Open Projects Fund Financed by Hangzhou Normal University (No. PDKF2010YG06)

First author biography: LIU Wangbing(1990—), male, master candidate. He majors in ocean color remote sensing studies. E-mail: luby138@126.com

Corresponding author biography: ZHOU Bin(1972—), male, Ph. D., professor. His research interests are case Ⅱ water color remote sensing, theory simulation and calculation of particle optical properties, error analysis and uncertainty evaluation of remote sensing products. He has published over 70 academic papers. E-mail: hznu_bzhou@126.com

atellite sensors, such as Advanced Land Imager (ALI) with different spectral and spatio-temporal resolutions, can be used in the inversion of water quality products (Chen, et al., 2004). Many existing studies have used Ocean color sensors (Hu, et al., 2004; Wang, et al., 2011; Chen, et al., 2011) and Landsat data (Hui, et al., 2008; Wu, et al., 2008; Chen, et al., 2009) for water quality monitoring. Although marine color sensors have short revisit time and high spectrum resolution and sensitivity, low space resolution of the data remains insufficient for elaboration of the water features in a meso-scale area such as those in the Hangzhou Bay (e.g., the highest spatial resolution of MODIS is 250 m). Land sensors, by contrast, have a higher space resolution but a much longer revisit time (e.g., Landsat TM has a visit cycle of 16 d), which also renders data as inconvenient for high dynamic water monitoring in Hangzhou Bay. Otherwise, the distribution and the density of different size particles of suspended sediments vary dramatically in different areas. Corresponding reflectance spectral characteristics also extremely change. Water spectral characteristics of different regions still lack research, especially for regional water bodies such as Hangzhou Bay (Wang, et al., 2009), which would not be conducive to the development of accurate remote sensing inversion.

The small satellite constellation, which included two stars (HJ-1A/1B star, hereinafter referred to as HJ star) that was successfully launched at 11:25 am on September 6, 2008, is a special satellite constellation for environmental monitoring and disaster prediction in China. The CCD cameras carried by the satellites can obtain reflectivity data from four spectral bands: 430—520 nm, 520—600 nm, 630—690 nm, and 760—900 nm. The amplitude sweep width is 360 km (two sensors combined is ≥700 km), the recorded data is 8 bits, and the signal-to-noise ratio is more than 48 dB, which are suitable for water quality monitoring in meso-scale regions. The constellation of two satellites with high spatial resolution (30 m) and the short revisit time (2 d) can provide multi-spectral CCD imaging (Li, et al., 2008). Based on the advantages of high spatio-temporal resolution of the HJ CCD image, this study analyzed the relationship between field Suspended Sediment Concentration (SSC) data and Remote Sensing Reflectance (R_{rs}). The high-precision retrieval model of the Hangzhou Bay based on the HJ CCD image for SSC quantitative analysis was then built.

2 RESEARCH DATA

2.1 Research area

Located in the northern part of the Zhejiang Province and south of Shanghai, Hangzhou Bay, with the geographical position of (29.92°N—30.86°N, 120.95°E—122.07°E), is a trumpet-shaped bay formed by the Qiantang River running into the sea. As the estuary of the Qiantang River and as the most famous bay in the world with strong tides, Hangzhou Bay has many significant characteristics such as strong tidal flow, weak runoff, and less sand accumulation from the inner land but more from the sea. Approximately 435 million tons (Datong Station, 1951—2000) of sediment from the Yangtze River pours into the sea annually, which partly diffuses south to the Hangzhou Bay. The sediment pass volume on the interfaces of the Yangtze River estuary and of the Hangzhou Bay is approximately 230 million tons, which are the main sources of sediment for Hangzhou Bay (Wu, et al., 2006). As a result of the strong tidal trend, a large portion of the area in Hangzhou Bay has a relatively high SSC.

2.2 Research data

HJ CCD data used in this study (false color composite image is shown in Fig. 1) were captured on December 12, 2011 at 10:39 am. The data were obtained from the website of the Chinese Resource Satellite Application Center.

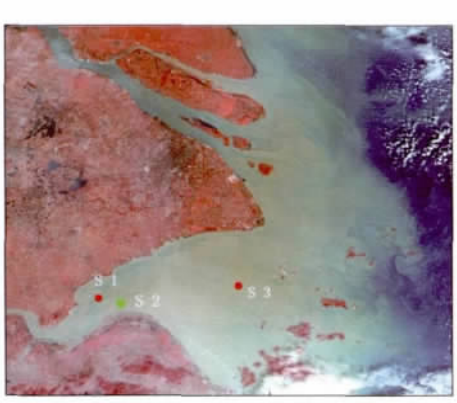

Fig. 1 The false color composite HJ CCD image of the Hangzhou Bay and of the distribution of field stations (S2: The synchronous field station, R: band 4; G: band 3; B: band 2)

In situ measured data in three field stations (S1, S2, and S3), including SSC and spectral data on December 2 and 13, 2011, within a complete tidal cycle were collected. The field data were synchronized with the HJ CCD image obtained at S2 (Andong) station (30.44°N, 121.19°E, Fig. 2) on December 12, 2011 when the sky was cloudless, the average wind speed was 1.8 m/s, and the water surface was relatively calm and had a few white hat.

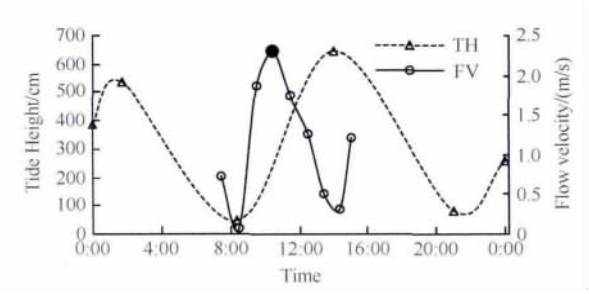

Fig. 2 Field velocity and tide height at Zhapu Station (The black point corresponds to the synchronization time)

2.2.1 The Flow Velocity Data

The tidal height data obtained from the Zhapu Port, where tidal isoline was close to the S2 site, conformed to the velocity data measured by the Acoustic Doppler Current Profilers (ADCP). The reason for this conformity is because the high tidal variation rate corresponds to the high flow velocity and vice versa. The HJ CCD image used in this research was captured at 10:39 am, when the velocity was fastest during the day. Due to the strong tides, the strong resuspension and movement of water mas-

ses with high sediment concentration may have contributed to the high SSC at Hangzhou Bay.

2.2.2 Spectrum Data

According to NASA SeaWiFS marine optical measurement specification, ASD spectrometer was used to measure spectral data, with 135° of the angle between the observation direction plane and the sun incident direction plane (integrated backscatter sun direction) and with 40° of the angle between the observation and the sea normal direction (Mueller & Austin, 1992; Tang, et al., 2004). The procedure was performed to measure the standard plate, the sky, and the surface in turn. In order to avoid the effects of human and hull shadows, the spectrometer was fixed horizontally by a triangular bracket, and the metal pole fixed with the probe was far from the hull at about 2.5 m. With the horizontal dial on the triangular bracket, the observation angle can be calculated from the shadows caused by the sunlight, to ensure correctness of the observation geometry. The field spectral data were filtered according to the sun elevation angle, and 49 pairs of available SSC and spectral data were finally obtained.

2.2.3 The Concentration Data

Water samples were collected using a Niskin sampler under the water surface at 5—10 cm, which was synchronized with the spectral measurements. The filtrate was then carried by the vacuum pump (swept volume of 30 L/min) using cellulose acetate membranes with 0.45 μm aperture, which was dried and pre-weighed on board. The filters were stored in a −20 ℃ refrigerator until subjected for processing in the laboratory for data analysis. As shown in Fig. 3, SSC data were collected every hour at the S2 station on December 12, 2011. SSC changed dramatically during the day, and the difference between the highest and the lowest concentrations was more than 1300 mg/L.

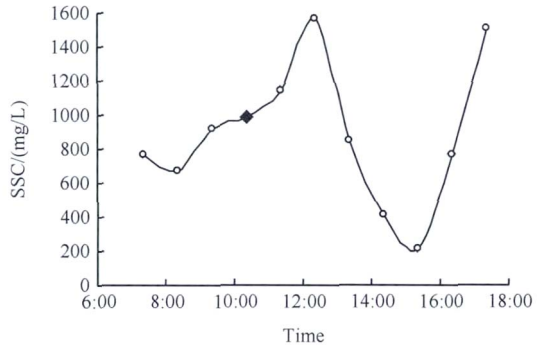

Fig. 3 SSC data at the S2 station on December 12, 2011 (The black point corresponds to the synchronization time)

2.3 Water body spectral characteristics of the Hangzhou Bay

The HJ CCD band settings and the field remote sensing reflectance curve obtained during the experiment at the Hangzhou Bay are shown in Fig. 4. Two reflectance peaks appeared at 630—690 nm of the third band and at 760—830 nm of the fourth band. The experiments of Han, et al. (2003) had shown that the reflectance spectrum of sandy water has two peaks, with the highest peak position at 600—700 nm, which is higher than the secondary one located at 760—820 nm when the sediment concentration is low, and the secondary peak increasing along with the sediment concentration. In this study, due to the high SSC of Hangzhou Bay, the secondary peak of the field remote sensing reflectance is high. The entire visible spectrum reflectivity elevates with the increase of SSC, while reflectance peaks at short wavelengths move toward the longer so-called "red-shift", which are consistent with existing research (Doxaran, et al., 2002; Han, et al., 2003).

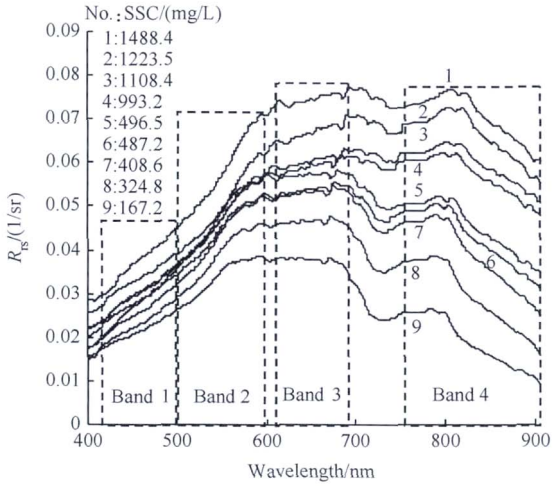

Fig. 4 Field spectral reflectance curves of Hangzhou Bay and the HJ CCD band settings

Through the correlation analysis between the field R_{rs} of water and the corresponding SSC data, the correlation coefficient curve of field R_{rs} and SSC was obtained as shown in Fig. 5.

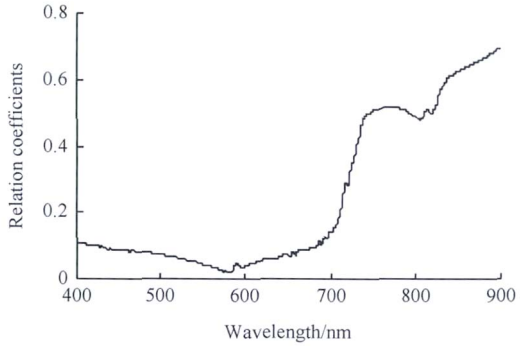

Fig. 5 Correlation coefficients of field R_{rs} and SSC

As shown in Fig. 5, in the wavelength range from 400 nm to 900 nm, the correlation coefficients are generally increasing. The curve shows a minimum correlation coefficient near 570 nm, and a small peak appears near 750 nm. Subsequently, the highest correlation coefficient value is achieved at 900 nm. Thus, the correlation coefficient of field R_{rs} and SSC during this voyage is higher at the relatively long wavelength. The curve shows that the lowest correlation coefficients near 570 nm may have been caused by high SSC at the Hangzhou Bay. As both the water reflectance at around 570 nm and SSC at the Hangzhou Bay are high, R_{rs} at 570 nm is less sensitive to the changes of sediment concentra-

tion. The correlation analysis can be used to the subsequent modeling of the remote sensing data.

3 SSC INVERSION MODEL OF THE HANGZHOU BAY

3.1 Calculation of the band equivalent value

The field data mainly contain SSC, remote sensing reflectance, and aerosol optical depth, among others. The validity of the data must be determined before molding. For example, the field spectral data that did not satisfy the required zenith angle must be removed. Before designing the inversion algorithm based on the HJ CCD band settings, HJ CCD band spectral r esponse function should be used to calculate the band equivalent value of the HJ CCD band spectral data.

The equation of the band equivalent value calculation is written below:

$$R_{rsi} = \frac{\int_{\lambda_1}^{\lambda_2} S_i(\lambda) R_{rs}(\lambda) \, d\lambda}{\int_{\lambda_1}^{\lambda_2} S_i(\lambda) \, d\lambda}$$

where R_{rsi} refers to the equivalent-band remote sensing reflectance, $R_{rs}(\lambda)$ refers to the in situ field remote sensing r eflectance, $S_i(\lambda)$ is the spectral response function, and λ_1 and λ_2 correspond to the 0.1% response points on both sides of the spectrum response function.

3.2 HJ CCD imaging atmospheric correction auxiliary with the MODIS aerosol data

Using the Near Infrared-Short Wave Infrared (NIR-SWIR) atmospheric correction method embedded in the SeaWiFS data a nalysis system (SeaDAS) (Shi & Wang, 2007), the synchronized aerosol optical thickness value of the Terra/MODIS image was obtained for the correction of the HJ CCD image. The imaging times of the HJ CCD imagery and of the quasi-synchronous Terra/MODIS on December 12, 2011 were 10:39 am and 10:05 am, respectively. As the time difference is about half an hour, we assume that the aerosol is nearly invariable. Hence, the Terra/MODIS aerosol data can be applied to the atmospheric correction of HJ CCD. The Aerosol Optical Depth (AOD) distribution of the Hangzhou Bay and of the adjacent waters was then obtained. The distribution shows that the most frequent AOD value for near 547 nm is 0.4168, and the corresponding visibility, which is 18.8 km, is calculated as the input parameters for the FLAASH atmospheric correction module in the ENVI software.

Using field remote sensing reflectance measured at 10:20 am and combined with the HJ CCD spectral response function, the band equivalent remote sensing reflectance of the four bands of HJ CCD was obtained , and the HJ CCD atmospheric correction results were then validated . The results show that the relative error of the HJ CCD atmospheric correction is relatively small at the third (5.54%) and at the fourth bands (6.97%) (Table 1). The accuracy of the measurements at the first and at the second bands, on the contrary, is poor. As shown in Fig. 6, the resulting accuracy of the atmospheric correction at the first, third, and fourth bands is higher than those in the field measured data, while that at the second band is lower. The atmospheric correction results at band 3 and band 4 can be used for the inversion of SSC.

Table 1 Accuracy evaluation of HJ CCD imaging atmospheric correction

HJ CCD	Band equivalent value R_{rs}	Atmospheric correction R_{rs}	R. E. /%
b1	0.0328	0.0429	30.75
b2	0.0482	0.0258	46.50
b3	0.0591	0.0624	5.54
b4	0.0579	0.0620	6.97

Note: R. E. represents Relative Error

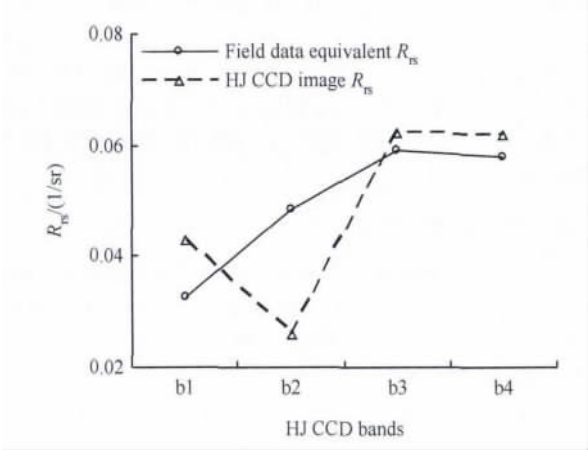

Fig. 6 Comparison between HJ CCD atmospheric correction results and field data equivalent reflectance

3.3 Inversion model of SSC with HJ CCD data

Based on the HJ CCD bands, the corresponding band e quivalent remote sensing reflectance was calculated, and the r emote sensing factor, such as single-band and in-band ratios, was built. Two-thirds of the total actual data were used for model building and one-third for validating. Through regression analysis, the retrieval models of relationship between various r emote sensing factors and SSC were established. The determination coefficient of the model R^2, Root Mean Square Error (RMSE), and Mean Relative Error (MRE) between the simulation results and the field data were calculated. As shown in Table 2, the factor built by the reflectance ratio between the fourth and the third bands demonstrated the best performance. The average relative error of the model was smallest, and the corresponding results of each validation data are shown in T able 3, in which MRE is 13.6%.

As mentioned above, the two reflection peaks of the Hangzhou Bay field spectra were in the third and in the fourth bands. Thus, based on their remote sensing reflectance, the third and the fourth bands are most sensitive to the changes of SSC, while their atmospheric correction has good results. Therefore, the SSC inversion model of the Hangzhou Bay, which was used in this research, is as below.

Table 2 The models and the validation results

Model	Remote sensing factor (X)	Model building data(33)	Validation data(16)		
		Fitting equation	R^2	RMSE/(mg/L)	MRE/%
Exponential model	R_{rs}(b1)	SSC = 393.89 × exp(15.129 × X)	0.02	474.8	62.26
Exponential model	R_{rs}(b2)	SSC = 431.15 × exp(7.8441 × X)	0.01	489.6	62.81
Exponential model	R_{rs}(b3)	SSC = 338.81 × exp(10.769 × X)	0.02	475.4	50.97
Exponential model	R_{rs}(b4)	SSC = 105.48 × exp(37.679 × X)	0.46	392.6	39.87
Exponential model	R_{rs}(b2)/R_{rs}(b1)	SSC = 26452 × exp(−2.425 × X)	0.07	451.2	57.53
Exponential model	R_{rs}(b3)/R_{rs}(b2)	SSC = 0.0039 × exp(9.7671 × X)	0.19	514.3	60.94
Exponential model	R_{rs}(b4)/R_{rs}(b2)	SSC = 17.498 × exp(3.4546 × X)	0.90	235.5	18.14
Exponential model	R_{rs}(b4)/R_{rs}(b3)	SSC = 13.895 × exp(4.5176 × X)	0.90	190.5	13.60

Table 3 The model built by b4/b3 remote sensing factor and the validation results

Validation data No.	Field value/(mg/L)	Model inversion Value/(mg/L)	R. E. /%	RMSE/(mg/L)	MRE/%
1	796.4	966.3	21.34	190.5	13.60
2	1274.4	1131.0	11.25		
3	253.0	251.2	0.71		
4	693.6	854.9	23.26		
5	496.0	536.2	8.10		
6	496.6	462.9	6.79		
7	228.6	278.4	21.80		
8	214.0	214.9	0.42		
9	1775.2	1275.3	28.16		
10	1571.2	1120.5	28.69		
11	1108.4	1173.9	5.91		
12	918.0	782.3	14.78		
13	993.2	1089.6	9.71		
14	852.0	878.3	3.09		
15	728.4	640.1	12.12		
16	368.6	289.6	21.44		

$$SSC = 13.895 \times \exp(4.5176 \times X)$$

SSC denotes suspended sediment concentration in units of mg/L and $X = R_{rs}(b4)/R_{rs}(b3)$, where $R_{rs}(b4)$ and $R_{rs}(b3)$, represents remote sensing reflectance of band 4 and band 3, respectively. Several models have already been developed by domestic scholars, such as the logarithmic model application to the Yangtze River (Chen, et al., 1991; Li, et al., 2001), the Gordon model (He, et al., 1999), and the negative index model for the Hangzhou Bay area (Li, 1987). In comparison with the model built in this study, the first two models mentioned are not suitable for high SSC regions, and the negative exponential model by Li (1987) is for the NOAA/AVHRR satellite and similarly has difficulty in expressing or showing higher order changes of high SSC areas (Liu, et al., 2006). Thus, all the above-mentioned models are not suitable for the present research. The exponential model proposed in this letter will provide reference for the SSC quantitative retrieval of specific satellite images at the Hangzhou Bay.

4 RESULTS AND DISCUSSIONS

4.1 Analysis of the regression relation between concentration and model

The regression relationships under a 0.01 significance level from the F-test are notable. The scattergram and the regression relation between the modeling point equivalent value of R_{rs} and SSC are shown in Fig. 7.

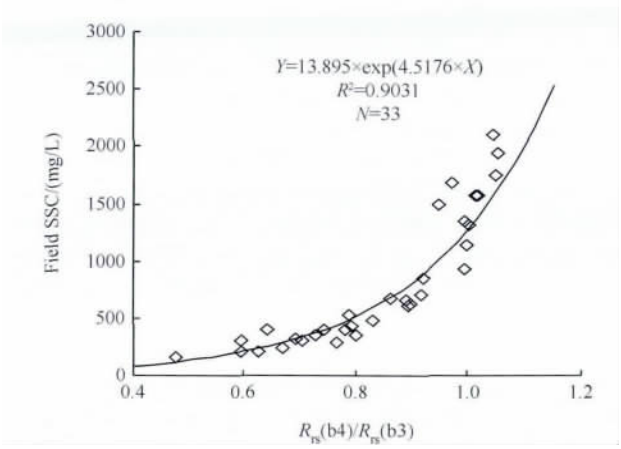

Fig. 7 Regression relationship between the field SSC and the field $R_{rs}(b4)/R_{rs}(b3)$

Fig. 8 exhibits the comparison between the HJ CCD algorithm simulation value and the field data, which demonstrates an ideal correlation.

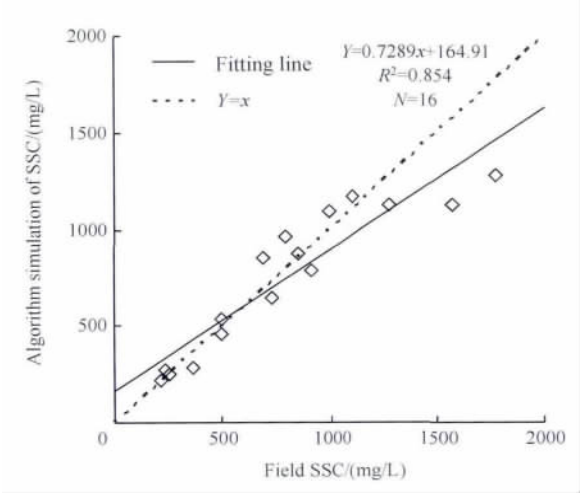

Fig. 8 Comparison between HJ CCD algorithm simulation SSC and the field data

4.2 Distribution of SSC at the Hangzhou Bay based on the band ratio exponential model

By using the built SSC inversion model to retrieve the HJ CCD image after atmospheric correction, the inversion result of SSC at the Hangzhou Bay was obtained and is shown in Fig. 9. The actual error and the average relative error of the field data used to validate the inversion results were 70.76 mg/L and 7.12%, respectively (Table 4). As illustrated in Fig. 9, SSC at the Hangzhou Bay is much higher than most areas in the Yangtze estuary, and the variation of the overall gradient is obvious.

Table 4 Validation of the inversion results

SSC/(mg/L)		A. E. /(mg/L)	R. E. /%
Field value	Inversion value		
993.20	1063.96	70.76	7.12

Note: A. E. means Actual Error

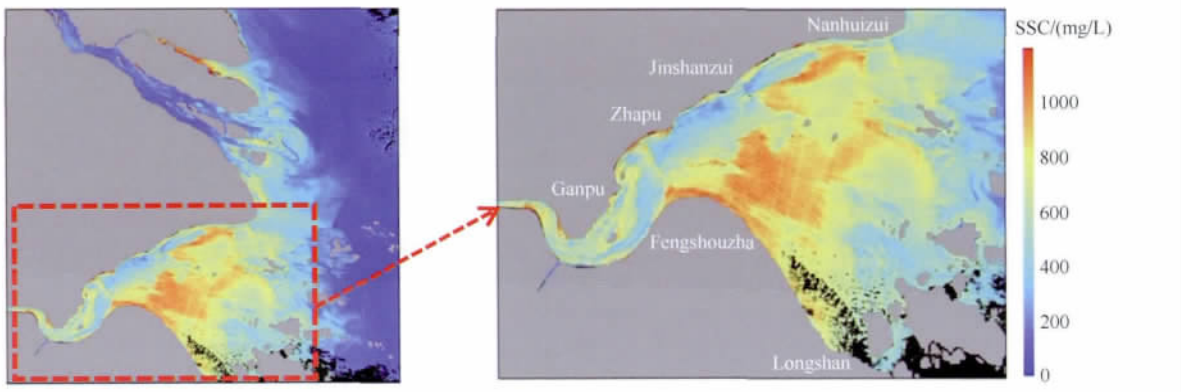

Fig. 9 SSC inversion results at the Hangzhou Bay and its adjacent waters
(Black portion is the area covered by clouds; grey area means land)

The field measurement was performed during a spring tide in winter. The high SSC and the significant internal variation can be observed from the inversion results over the entire Hangzhou Bay. The concentration gradually decreased from the central region, where the highest SSC appeared, to the inner bay and the open sea. Distribution of suspended sediments at the Hangzhou Bay estuary was mainly high in the north and low in the south. One of the high SSC regions appeared near Nanhui, in the northern part of the bay, and declined gradually to the southwest, which reflects the effect of sediment in the Changjiang River running into sea through the Hangzhou Bay. SSC in the middle section of the bay, which ranged from Jinshan to the Fengshouzha, was high in the south and low in the north. High SSC appeared in most regions of the Andong shoal, while low SSC was observed in a portion of the northern deep region. A high level of SSC at the bay head was obtained due to the strong tidal current. Two areas with low sediment concentration were formed at the deep trough along the north shore near JinShan and at the inlet in the east of LongShan. The concentration level in the former was mainly due to the weak resuspension caused by deeper waters, and that in the latter was mainly contributed by the high velocity of rising tides, which resulted in a large amount of clean water from the open sea running into the bay during measurement, leading to lower SSC at the interface between Hangzhou Bay and the open sea, as well as at the convergence within the Bay.

5 CONCLUSIONS

Field spectral data and the HJ CCD image data are used in this study for the quantitative inversion of SSC at the Hangzhou Bay. The so-called "red-shift", a phenomenon in which the field maximum curve peak of the remote sensing reflectance moves toward the longer wavelength while SSC increased, is found to occur at the Hangzhou Bay. Based on the equivalent reflectance ratio of the fourth and of the third bands at the reflection peak of HJ CCD, the exponential inversion model of SSC was built, and the determination coefficient was above 0.9. Inversion results indicate that the model can sufficiently describe the spatial distribution of SSC at the Hangzhou Bay and that domestic HJ CCD satellite image data can be used for ocean color remote sensing study in offshore regions in China. Results of this study can complement the inadequacy of the spectral research on the Hangzhou Bay and can serve as a reference for future study on the regional model of remote sensing inversion. The research will likewise have an important theoretical and practical significance not only

for the monitoring of small and medium-scale water quality, but also for subsequent development of the constellation.

Acknowledgements: Field data were collected with the a ssistance of Dou Wenjie, Li Fan, Yuan Xiaohong, and Zhou Fangfang from the Institute of Remote Sensing and Earth Sciences, Hangzhou Normal University, and the HJ CCD image data and auxiliary parameter were obtained from the Resource Satellite Application Center. We would like to express our sincere gratitude.

REFERENCES

Chen M, Li S H and Liu X J. 1991. Processing and analyzing suspended sediment remote sensing information of the Yangtze estuary. Journal of Hydraulic Engineering, 5(5): 47 - 51

Chen S S, Fang L G, Zhang L X and Huang W R. 2009. Remote sensing of turbidity in seawater intrusion reaches of Pearl River Estuary - a case study in Modaomen water way, China. Estuarine, Coastal and Shelf Science, 82(1): 119 - 127 [DOI: 10.1016/j.ecss.2009.01.003]

Chen S S, Huang W R, Chen W Q and Wang H Q. 2011. Remote sensing analysis of rainstorm effects on sediment concentrations in Apalachicola Bay, USA. Ecological Informatics, 6(2): 147 - 155 [DOI: 10.1016/j.ecoinf.2010.12.001]

Chen X L, Li Y S, Liu Z G, Yin K D, Li Z L, Wai O W H and King B. 2004. Integration of multi-source data for water quality classification in the Pearl River estuary and its adjacent coastal waters of Hong Kong. Continental Shelf Research, 24(16): 1827 - 1843 [DOI: 10.1016/j.csr.2004.06.010]

Cheng T W and Zhao C N. 1985. The influence to the coast of our country main land stream runoff and sediment discharge. Acta Oceanologica Sinica, 7(4): 460 - 471

Doxaran D, Froidefond J M, Lavender S and Castaing P. 2002. Spectral signature of highly turbid waters-Application with SPOT data to quantify suspended particulate matter concentrations. Remote Sensing of Environment, 81(1): 149 - 161 [DOI: 10.1016/S0034 - 4257(01)00341 - 8]

Gin K Y H, Koh S T and Lin L L. 2003. Spectral irradiance profiles of suspended marine clay for the estimation of suspended sediment concentration in tropical waters. International Journal of Remote Sensing, 24(16): 3235 - 3245 [DOI: 10.1080/01431160110114934]

Han Z, Yun C X and Jiang X Z. 2003. Experimental study on reflected spectrum of suspended sediment. Journal of Hydraulic Engineering, (12): 118 - 122

He Q, Yun C X and Shi W R. 1999. Remote sensing analysis of the Yangtze estuary surface water suspended sediment concentration. Progress in Natural Science, 9(2): 160 - 164

Hu C M, Chen Z Q, Clayton T D, Swarzenski P, Brock J C and Muller-Karger F E. 2004. Assessment of estuarine water-quality indicators using MODIS medium-resolution bands: Initial results from Tampa Bay, FL. Remote Sensing of Environment, 93(3): 423 - 441 [DOI: 10.1016/j.rse.2004.08.007]

Hui F M, Xu B, Huang H B, Yu Q and Gong P. 2008. Modeling spatial-temporal change of Poyang Lake using multitemporal Landsat imagery. International Journal of Remote Sensing, 29(20): 5767 - 5784 [DOI: 10.1080/01431160802060912]

Li C R, Jia Y Y, Hu J and Li Z Y. 2008. An analysis of the prospects of HJ-1 optical satellites in remote sensing application. Remote Sensing for Land and Resources, (3): 1 - 3, 9

Li J. 1987. Assessment of suspended sediment concentration in Hangzhou Bay using NOAA/AVNRR imagery. Acta Oceanologica Sinica, 9(1): 132 - 135

Li S H. 2001. The Remote Sensing Mechanism and Applications of Ocean Color in Coastal Area. Shanghai: East China Normal University

Liu Z G, Zhou Y X, Jiang X Z and Shen F. 2006. Progress on suspended sediment concentration remote sensing in nearshore case 2 waters. Progress in Geophysics, 21(1): 321 - 326

Morel A and Prieur L. 1977. Analysis of variations in ocean color. Limnology and Oceanography, 22(4): 709 - 722 [DOI: 10.4319/lo.1977.22.4.0709]

Mueller J L and Austin R W. 1995. Ocean Optics Protocols for SeaWiFS Validation (NASA Technical Memo 104566) vol 25 (Greenbelt, MD: NASA GSFC) p 24

Tang J W, Tian G L, Wang X Y, Wang X M and Song Q J. 2004. The methods of water spectra measurement and analysis I: above-water method. Journal of Remote Sensing, 8(1): 37 - 44

Tassan S. 1997. A numerical model for the detection of sediment concentration in stratified river plumes using Thematic Mapper data. International Journal of Remote Sensing, 18(12): 2699 - 2705 [DOI: 10.1080/014311697217567]

Wang F, Zhou B, Xu J M, Ling Z Y and Zhou G D. 2009. Surface spectral measurement and characteristics analysis of turbid water in Hangzhou bay. Spectroscopy and Spectral Analysis, 29(3): 730 - 734

Wang M H and Shi W. 2007. The NIR-SWIR combined atmospheric correction approach for MODIS ocean color data processing. Optics Express, 15(24): 15722 - 15733 [DOI: 10.1364/OE.15.015722]

Wang M H, Shi W and Tang J W. 2011. Water property monitoring and assessment for China's inland Lake Taihu from MODIS-Aqua measurements. Remote Sensing of Environment, 115(3): 841 - 854 [DOI: 10.1016/j.rse.2010.11.012]

Wu G F, De Leeuw J, Skidmore A K, Prins H H T and Liu Y L. 2008. Comparison of MODIS and Landsat TM5 images for mapping tempo-spatial dynamics of Secchi disk depths in Poyang Lake national nature reserve, China. International Journal of Remote Sensing, 29(8): 2183 - 2198 [DOI: 10.1080/01431160701422254]

Wu H L, Shen H T, Yan Y X and Wang Y H. 2006. Preliminary study on sediment flux into the sea from Changjiang Estuary. Journal of Sediment Research, (6): 75 - 81

杭州湾 HJ CCD 影像悬浮泥沙遥感定量反演

刘王兵[1]，于之锋[2,3]，周斌[2]，蒋锦刚[2]，潘玉良[2]，凌在盈[2]

1. 浙江大学 遥感与信息技术应用研究所,浙江 杭州 310058;
2. 杭州师范大学 遥感与地球科学研究院,浙江 杭州 311121;
3. 武汉大学 测绘遥感信息工程国家重点实验室,湖北 武汉 430079

摘 要: 利用环境小卫星 CCD(HJ CCD)影像对杭州湾悬浮泥沙浓度(SSC)进行了反演研究。通过对杭州湾水体遥感反射率(R_{rs})与 SSC 进行相关性分析发现,在 690 nm 和 830 nm 左右出现显著的反射峰,分别位于 HJ CCD 影像的第 3 和第 4 波段范围内;大于 700 nm 波长处的 R_{rs} 与 SSC 相关性较好。基于实测 R_{rs} 和 SSC 之间的相关关系,利用第 4 和第 3 波段比值作为遥感因子建立 SSC 反演模型,模型决定系数达到 0.90。借鉴近红外-短波红外(NIR-SWIR)结合的大气校正方法反演出的准同步 MODIS 气溶胶数据,实现了 HJ CCD 影像的大气校正,第 3、第 4 波段的大气校正结果相对误差分别为 5.54% 和 6.97%。结果显示,HJ CCD 影像反演的 SSC 相对误差为 7.12%;杭州湾悬浮泥沙浓度要显著高于长江口,且内部差异明显。研究表明,通过适当的大气校正方法和反演算法,HJ CCD 影像可用于杭州湾悬浮泥沙浓度的估计。

关键词: HJ CCD,杭州湾,悬浮泥沙浓度,遥感反射率,大气校正

中图分类号: TP79 **文献标志码**: A

引用格式: 刘王兵,于之锋,周斌,蒋锦刚,潘玉良,凌在盈. 2013. 杭州湾 HJ CCD 影像悬浮泥沙遥感定量反演. 遥感学报,17(4):905-918

Liu W B, Yu Z F, Zhou B, Jiang J G, Pan Y L and Ling Z Y. 2013. Assessment of suspended sediment concentration at the Hangzhou Bay using HJ CCD imagery. Journal of Remote Sensing, 17(4): 905-918 [DOI: 10.11834/jrs.20132195]

1 引 言

受陆源影响比较大的Ⅱ类水体主要分布在近岸和河口区域(Morel 和 Prieur,1977)。随着近岸和沿海经济的快速发展,水体污染状况越发严重。悬浮泥沙是构成Ⅱ类水体光谱特性的重要水色要素和水质参数之一。水体中悬浮泥沙含量的大小不仅直接影响着水体的透明度、浑浊度、水色等光学性质,以及水生条件和河道、海岸带冲淤变化过程(程天文和赵楚年,1985),而且悬浮泥沙携带的大量污染物还是影响近海和内陆水体水质的重要因素之一(Tassan,1997)。传统的水质监测方法是进行定期的野外实测取样,不仅耗财费时,数据量少,而且很难进行大区域的时空变化监测。因此,需要一种能提供水质生物光学指标长时序观测的监测工具。

遥感以其特有的空间和时间优势,成为了大面积水质动态监测的有效手段和工具(Gin 等,2003)。如今水色传感器例如 Coastal Zone Color Scanner(CZCS)、Sea-viewing Wide Field-of-view Sensor(SeaWiFS),Medium Resolution Imaging Spectrometer(MERIS)和 Moderate Resolution Imaging Spectroradiometer(MODIS);陆地卫星传感器例如 Advanced Land Imager(ALI),具有不同的光谱和时空分辨率,都能反演出水质数据产品(Chen 等,2004)。已有研究使用海洋水色传感器(Hu 等,2004; Wang 等,2011; Chen 等,2011)和陆地卫星数据(Hui 等,2008; Wu 等,2008; Chen 等,2009)进行水质监测。虽然海洋水色传感器有短回访周期、高光谱分辨率

收稿日期: 2012-06-27; 修订日期: 2012-10-23; 优先数字出版日期: 2012-10-30

基金项目: 国家自然科学基金(编号: 40971193; 41206169; 41206168);海洋公益性行业科研专项(编号: 200905012; 201005030);杭州师范大学遥感与地球科学研究院开放基金(编号: PDKF2010YG06)

第一作者简介: 刘王兵(1990—),男,硕士研究生,研究方向为水色遥感。E-mail: luby138@126.com

通信作者简介: 周斌(1972—),男,博士,教授。现主要从事二类水体水色遥感、颗粒物光学性质的理论模拟和计算、遥感产品等空间数据的误差分析及不确定性评价等方向的研究,已发表论文 70 余篇。E-mail: hznu_bzhou@126.com

和高灵敏度的特点,但其较低的空间分辨率还不能充分描述小尺度区域的水质特征(例如,MODIS 最高的空间分辨率为 250 m);陆地传感器空间分辨率较高,但回访周期较长(例如,Landsat TM 的回访周期是 16 d),使得这些数据都不利于杭州湾高动态水体水质变化的监测。另外,由于不同水域悬浮泥沙粒径分布和浓度的不同,其相应的反射率光谱特性也有所差异,目前国内对不同区域水体光谱特征还缺乏全面的把握,尤其是对杭州湾水域的水体光谱研究较少(王繁 等,2009),不利于准确的区域化遥感反演算法的发展。

环境与灾害监测预报小卫星星座 A 星、B 星(HJ-1A/1B 星,以下简称 HJ 星)于 2008 - 09 - 06 11:25 成功发射,是中国环境与灾害监测预报的专用卫星。卫星上携带的 CCD 相机可以获得 4 个光谱波段(430—520 nm,520—600 nm,630—690 nm 和 760—900 nm)的反射率数据,扫幅宽度为 360 km(两个传感器≥700 km),记录 8 bits 数据,信噪比≥48 dB,适用于中、小尺度区域的大范围覆盖监测。两颗卫星组成的星群能生成具有高空间分辨率(30 m)和短回访时间(2 d)的多光谱 CCD 影像(李传荣 等,2008)。本研究将利用 HJ CCD 影像较高时空分辨率的优势,通过分析实测 SSC 和 R_{rs} 数据之间的关系,建立基于 HJ CCD 影像的杭州湾 SSC 高精反演模型,对杭州湾水域的悬浮泥沙浓度分布进行定量分析。

2 研究区和实测数据

2.1 杭州湾概况

杭州湾位于浙江省中北部,上海市南部,地理坐标为(29.92°N—30.86°N,120.95°E—122.07°E),是钱塘江入海形成的一个喇叭形海湾。作为钱塘江入海口、世界上著名的强潮型河口湾,杭州湾具有潮流强、径流弱、陆域来沙少和海域来沙丰富等特征,每年约有 4.35 亿 t(大通站,1951 年—2000 年)的泥沙从长江口倾注入海,其中部分泥沙南下扩散进入杭州湾(长江口与杭州湾界面泥沙通量约为 2.30 亿 t),成为杭州湾海域泥沙的主要来源(吴华林 等,2006)。由于潮流作用强烈,杭州湾大部分区域 SSC 都比较高。

2.2 数据获取

本研究使用的 HJ CCD 影像数据(影像假彩色见图 1)的成像时间为 2011 - 12 - 12 10:39 am,数据来源于中国资源卫星应用中心网站。

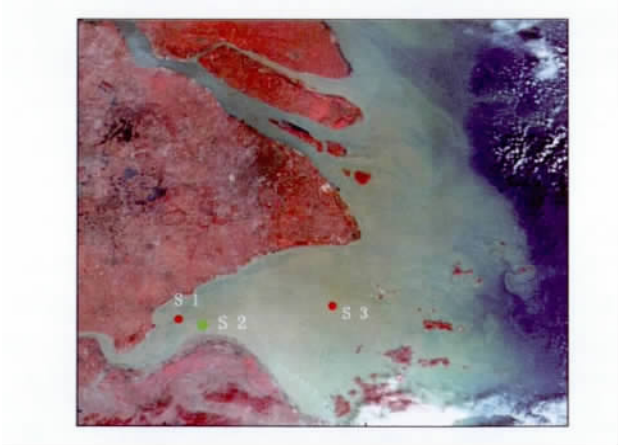

图 1 2011 - 12 - 12 杭州湾 HJ CCD 假彩色合成图和实测数据站位分布
(绿色标记 S2 为本研究实测数据对应点位,R: 第 4 波段; G: 第 3 波段; B: 第 2 波段)

现场数据采集主要包括 3 个实测站点(S1,S2 和 S3)实地悬浮泥沙浓度和光谱数据对的采集,采样时间从 2011 - 12 - 02 到 2011 - 12 - 13,跨越完整的大、中、小潮周期。其中与本研究所用环境星同步的实测数据为 2011 - 12 - 12 获取的庵东 S2 号站点(30.44°N,121.19°E,图 2)数据,数据获取当天,天空晴朗无云,平均风速为 1.8 m/s,水面波浪较小,观测区内无明显白帽。

2.2.1 流速数据

由于 S2 站点位于乍浦港潮差等值线附近,所以由乍浦港获取的潮高数据和实验中所测得的流速流向仪(ADCP)数据对应良好,主要表现为: 涨憩落憩时,流速最慢; 涨急落急时,流速最快。HJ CCD 影像成像时刻为 10:39 am,由图 2 可以看出,此时该点位处于一天内流速最快时段,所以由于快速的潮流引起的泥沙再悬浮作用及高泥沙浓度水团的移动都可能成为高悬浮泥沙浓度的成因。

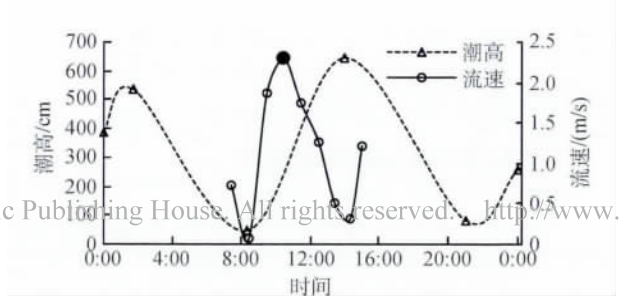

图 2 实测点位流速及当日乍浦站潮高图

2.2.2 光谱数据

根据 NASA SeaWiFS 海洋光学测量规范(Mueller 和 Austin,1992)与唐军武等人(2004)提出的水面之上测量法,使用 ASD 地物光谱仪,采用(40°,135°)的观测角度,即仪器观测平面与太阳入射平面的夹角为 135°(背向太阳方向),仪器与海面法线方向的夹角为 40°,依次对标准板、天空和水面进行测量。光谱仪采用三角支架进行水平固定,将带有探头的撑杆伸出船体约 2.5 m 左右,以避免人体及船体阴影的影响,通过水平支架上装配垂直指针的刻度盘,可以根据太阳阴影确定观测的角度,以保证观测几何的正确性。再根据太阳高度角对已测得的光谱数据进行筛选,最终获得采样期间有效的悬浮泥沙浓度和光谱数据 49 对。

2.2.3 浓度数据

水样采集与光谱测量同步进行,水样采集取水表面以下 5—10 cm 处的表层水。为保证实验的科学性和精确性,样品采用孔径为 0.45 μm 的醋酸纤维滤膜,利用抽气量为 30 L/min 的真空泵进行现场过滤。过滤后的滤膜放入液氮罐中保存,待实验结束后,带回实验室进行烘干、灼烧和称量分析。图 3 显示的是 2011 – 12 – 12 S2 站位每隔 1 h 采集的悬浮泥沙浓度数据,从图中可以发现,该站点的 SSC 在一天之内变化显著,最高和最低浓度之差超过 1 300 mg/L。

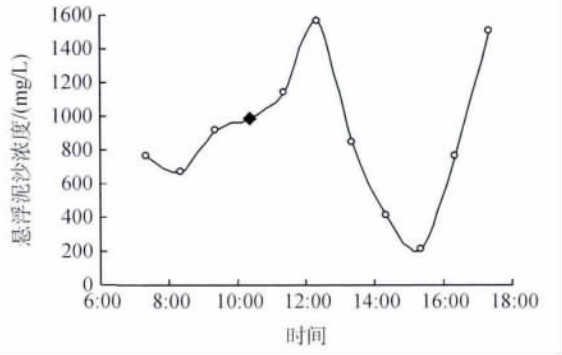

图 3 2011 – 12 – 12 对应站点的 SSC 数据
(黑色实心点为 HJ CCD 影像同步时刻数据)

2.3 杭州湾水体光谱特征分析

2011 年 12 月实验期间获取的部分杭州湾水体实测遥感反射率曲线、对应的泥沙浓度数据以及 HJ CCD 波段设置如图 4 所示。在第 3 波段的 630—690 nm 和第 4 波段的 760—830 nm 附近出现两个反射峰。韩震等人(2003)的实验表明含沙水体的反射率光谱有两个峰值:主峰位置在 600—700 nm,次级峰位于 760—820 nm,含沙量较低时,主峰高于次级峰,随着含沙量增加,次级峰的反射率逐渐升高。本次杭州湾实验实测点的 SSC 大部分时间内都处在较高水平,故次级峰均较高。随着 SSC 的增加,整个可见光谱段的反射率增加,同时反射峰值由短波逐渐向长波方向移动,即“红移现象”,这与已有的研究相吻合(Doxaran 等,2002;韩震 等,2003)。

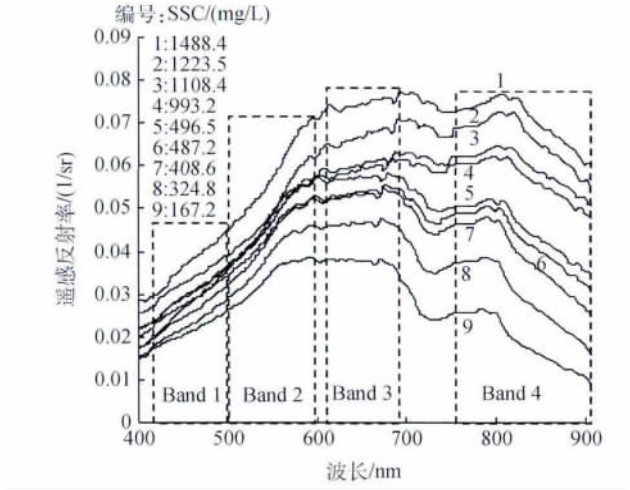

图 4 杭州湾实测遥感反射率曲线和 HJ CCD 波段范围

通过对实验中所获取的水体遥感反射率与对应悬浮泥沙浓度数据进行相关性分析,得到实测水体 R_{rs} 与 SSC 的相关性关系(图 5)。

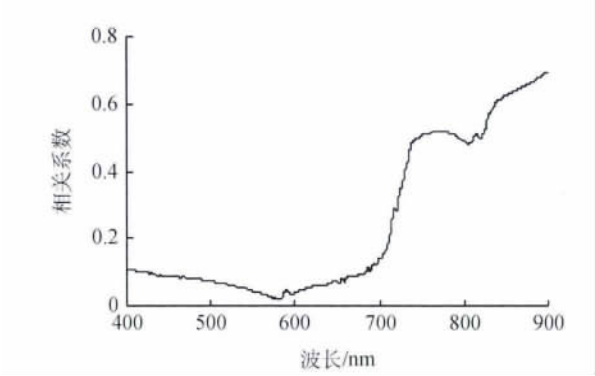

图 5 实测水体 R_{rs} 和 SSC 的相关系数图

由图 5 可以看出,在波长 400—900 nm 区间内,与之对应的相关系数总体呈现升高的趋势,在 570 nm附近相关系数最小,在 750 nm 附近出现一个波峰,900 nm 处达到相关系数的最高值。由此可见,本航次杭州湾实测水体 R_{rs} 和 SSC 在较长波长处相关性较好。在 570 nm 附近的相关性较低,这可能

与杭州湾高悬浮泥沙浓度有关。由于含沙水体在 570 nm 左右的反射率较其他波段高,而杭州湾的悬浮泥沙浓度也比较高,因此,该波长处的遥感反射率对泥沙浓度变化的敏感度较低。该相关性分析可为后续遥感实测数据建模提供参考。

3 杭州湾水体 SSC 反演模式

3.1 波段等效值计算

实验获取的实测数据主要有悬浮泥沙浓度、水体的遥感反射率和大气气溶胶光学厚度等。在利用实测数据建模之前,首先需要对数据的有效性进行判定,剔除异常数据,例如不满足太阳天顶角要求的实测光谱数据都需要剔除,不参与建模。在设计反演算法之前,根据 HJ CCD 的波段设置,利用 HJ CCD 各波段的光谱响应函数对实测光谱数据进行波段等效值计算。

波段等效值的计算方法如下:

$$R_{rsi}=\frac{\int_{\lambda_1}^{\lambda_2} S_i(\lambda)\,R_{rs}(\lambda)\,d\lambda}{\int_{\lambda_1}^{\lambda_2} S_i(\lambda)\,d\lambda}$$

式中,R_{rsi}为等效波段遥感反射率; $R_{rs}(\lambda)$ 为各站位实测光谱遥感反射率; $S_i(\lambda)$ 为光谱响应函数; λ_1、λ_2 分别对应光谱响应函数两侧 0.1% 的响应点。

3.2 MODIS 气溶胶辅助下的杭州湾 HJ CCD 影像大气校正

利用 SeaWiFS 数据分析系统(SeaDAS)中嵌入的近红外 - 短波红外(NIR-SWIR)结合的大气校正方法(Wang 和 Shi,2007)得到对应时刻 Terra/MODIS 影像的气溶胶光学厚度值,用来校正同步的 HJ CCD 影像。2011 年 12 月 12 日 HJ CCD 影像与准同步的 Terra/MODIS 影像的成像时间分别为 10:39 am和 10:05 am,时间相差约 0.5 h,气溶胶变化较小,可将 Terra/MODIS 的气溶胶数据应用于 HJ CCD 的大气校正。反演得到杭州湾及其临近水体的气溶胶光学厚度(AOD)分布,统计出 547 nm 处出现频率最高的 AOD 为 0.4168,最后计算得出对应的能见度为 18.8 km,并将此数据作为 ENVI 软件中 FLAASH 大气校正模块的输入参数,来对影像进行大气校正。

利用 10:20 am 左右采集的杭州湾水体遥感反射率,结合 HJ CCD 的光谱响应函数,经计算获得与 HJ CCD 4 个通道对应的波段等效遥感反射率数据,然后对 HJ CCD 的大气校正结果进行验证。表 1 显示了 HJ CCD 影像大气校正精度评价结果,其中,HJ CCD 第 3 和第 4 波段的大气校正结果相对误差较小,分别是 5.54% 和 6.97%,第 1 和第 2 波段的大气校正结果精度较差。从图 6 中可以看出,第 1、3 和 4 波段的大气校正结果高于实测数据,第 2 波段低于实测数据。第 3 和第 4 波段的大气校正结果可用于悬浮泥沙浓度的反演。

表 1 HJ CCD 影像大气校正结果精度评价

HJ CCD	实测值波段等效 R_{rs}	大气校正后影像 R_{rs}	R. E. /%
b1	0.0328	0.0429	30.75
b2	0.0482	0.0258	46.50
b3	0.0591	0.0624	5.54
b4	0.0579	0.0620	6.97

注: R. E. 为相对误差

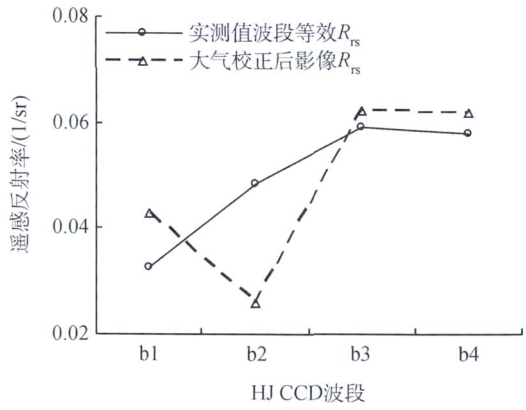

图 6 HJ CCD 影像大气校正结果与实测波段等效遥感反射率对比图

3.3 HJ CCD 影像悬浮泥沙浓度反演模型建立

按照 HJ CCD 波段设置计算相应波段的等效遥感反射率,并构建出单波段和波段比值遥感因子。实测有效数据中的三分之二用来建立模型,三分之一用来验证结果。通过回归分析,分别建立各遥感因子与悬浮泥沙浓度之间的反演模型,并求解出模型决定系数 R^2、均方根误差 RMSE、悬浮泥沙浓度算法模拟值和实测值之间的平均相对误差 MRE。由表 2 中的回归结果可以看出,第 4 波段和第 3 波段遥感反射率比值所构成的遥感因子表现最优,所构建反演模型的平均相对误差最小,相应的各个验证数据对的计算结果见表 3,MRE 为 13.60%。

表 2 实测悬浮泥沙浓度和 HJ CCD 波段等效遥感反射率数据建模及验证结果

模型	遥感因子(X)	建模数据(33 个)	验证数据(16 个)		
		拟合方程	R^2	RMSE/(mg/L)	MRE/%
指数模型	R_{rs}(b1)	SSC = 393.89 × exp(15.129 × X)	0.02	474.8	62.26
指数模型	R_{rs}(b2)	SSC = 431.15 × exp(7.8441 × X)	0.01	489.6	62.81
指数模型	R_{rs}(b3)	SSC = 338.81 × exp(10.769 × X)	0.02	475.4	50.97
指数模型	R_{rs}(b4)	SSC = 105.48 × exp(37.679 × X)	0.46	392.6	39.87
指数模型	R_{rs}(b2)/R_{rs}(b1)	SSC = 26452 × exp(−2.425 × X)	0.07	451.2	57.53
指数模型	R_{rs}(b3)/R_{rs}(b2)	SSC = 0.0039 × exp(9.7671 × X)	0.19	514.3	60.94
指数模型	R_{rs}(b4)/R_{rs}(b2)	SSC = 17.498 × exp(3.4546 × X)	0.90	235.5	18.14
指数模型	R_{rs}(b4)/R_{rs}(b3)	SSC = 13.895 × exp(4.5176 × X)	0.90	190.5	13.60

表 3 以第 4、第 3 波段比值组合作为遥感因子的反演模型各个验证数据对计算结果

验证数据对	实测值/(mg/L)	模型反演值/(mg/L)	R. E. /%	RMSE/(mg/L)	MRE/%
1	796.4	966.3	21.34	190.5	13.60
2	1274.4	1131.0	11.25		
3	253.0	251.2	0.71		
4	693.6	854.9	23.26		
5	496.0	536.2	8.10		
6	496.6	462.9	6.79		
7	228.6	278.4	21.80		
8	214.0	214.9	0.42		
9	1775.2	1275.3	28.16		
10	1571.2	1120.5	28.69		
11	1108.4	1173.9	5.91		
12	918.0	782.3	14.78		
13	993.2	1089.6	9.71		
14	852.0	878.3	3.09		
15	728.4	640.1	12.12		
16	368.6	289.6	21.44		

由于本次杭州湾实测光谱的两个反射峰分别位于第 3、第 4 波段,说明第 3 和第 4 波段的遥感反射率对浓度变化最为敏感,且第 3、第 4 波段的大气校正结果较好,因此,本研究杭州湾 SSC 反演所采用的悬浮泥沙浓度反演模型为:

$$SSC = 13.895 \times \exp(4.5176 \times X)$$

式中,$X = R_{rs}(b4)/R_{rs}(b3)$,$R_{rs}(b4)$ 和 $R_{rs}(b3)$ 分别表示第 4 波段和第 3 波段的遥感反射率。该模型与已有的应用到长江口等地区的对数模型(陈鸣 等,1991;李四海,2001)、Gordon 模型(何青 等,1999)以及针对杭州湾地区提出的负指数模型(李京,1987)相比,前两种通用模型均不适合于高浓度悬浮泥沙区域,而李京(1987)提出的负指数模型针对的是 NOAA/AVHRR 卫星,同样难以表达出高浓度悬沙区的高阶变化(刘志国 等,2006),所以以上模型均不适用于本研究。该指数模型的提出可为杭州湾地区今后特定卫星影像的悬浮泥沙定量反演模式提供借鉴和参考。

4 结果与讨论

4.1 浓度与模型回归关系分析

经 F 检验,该回归关系在 0.01 的显著性水平下是显著的。建模点的等效 R_{rs} 和实测 SSC 的散点图

及回归关系见图 7。

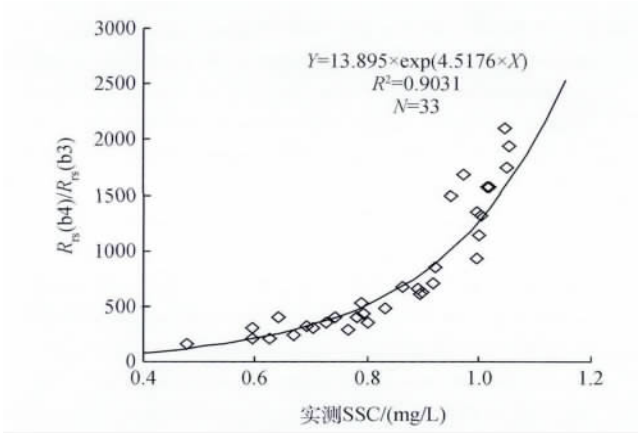

图 7 杭州湾建模点站位实测 SSC 与实测 R_{rs}(b4)/R_{rs}(b3)之间的回归关系

图 8 显示了悬浮泥沙浓度 HJ CCD 算法模拟值与实测值的比较,结果表明算法模拟值与实测值有很好的相关性。

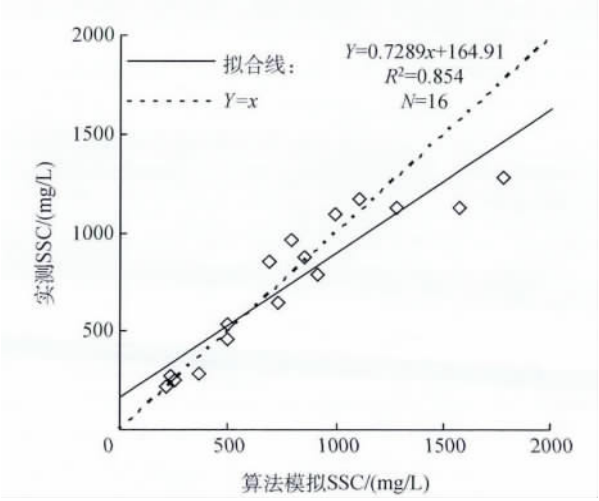

图 8 悬浮泥沙浓度 HJ CCD 算法模拟值和实测值的比较

4.2 基于波段比值指数模型的杭州湾泥沙浓度分布

利用建立的悬浮泥沙浓度反演模型对经过大气校正后的 HJ CCD 影像进行反演,得到杭州湾及邻近水域的 SSC 反演结果如图 9 所示。同时用实测站点数据对反演结果进行验证,实际误差为 70.76 mg/L,相对误差为 7.12%(表 4)。图 9 可以看出,杭州湾整体的 SSC 远高于长江口大部地区,且整体的变异梯度明显。

表 4 HJ CCD 影像泥沙反演结果验证

悬浮泥沙浓度/(mg/L)		A. E. /(mg/L)	R. E. /%
站点实测	HJ CCD 反演值		
993.20	1063.96	70.76	7.12

注: A. E. 为实际误差

影像同步时刻的杭州湾正处于冬季的一个大潮期间,由反演结果可以看出,杭州湾整体 SSC 普遍较高,内部差异明显,其中中部地区 SSC 最高,分别逐渐向湾口以里和外海递减。杭州湾湾口悬浮泥沙分布主要特点是北部高、南部低。北部南汇嘴附近出现一个高含沙区,由此向西南递减,这个高含沙区体现了长江入海泥沙对杭州湾的影响。杭州湾中部金山到丰收闸断面悬浮泥沙浓度南部高、北部低,庵东浅滩大部区域 SSC 都比较高,北岸深槽出现部分低浓度区域。由于潮差较大,潮流作用向湾顶聚集,使得该区域悬浮泥沙浓度较高。金山附近的北岸深槽和龙山以东的湾口水域形成两个低浓度含沙区。前者主要由于水体较深,再悬浮作用影响较小,故导致泥沙含量较低; 后者由于此时涨潮流速较大,大量的外海清洁或者较清洁水体进入杭州湾,所以导致杭州湾与外海接口处悬浮泥沙浓度较低,且整体的悬浮泥沙分布有向湾内汇聚的趋势。

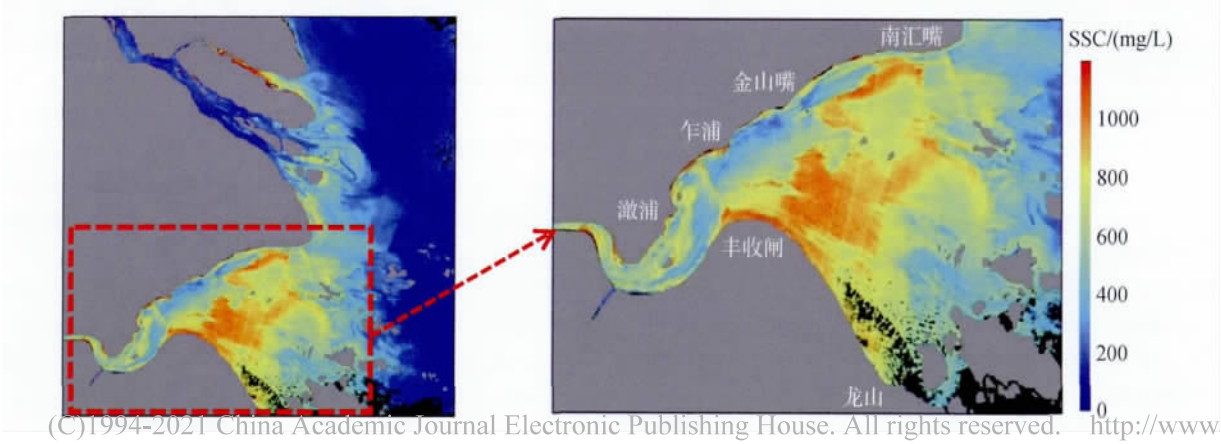

图 9 杭州湾及其邻近水体 HJ CCD 影像悬浮泥沙浓度反演结果
(黑色部分表示被云覆盖区域,灰色部分表示陆地)

5 结 论

利用实测光谱数据和 HJ CCD 影像数据对杭州湾悬浮泥沙进行定量研究。在杭州湾区域,实测遥感反射率曲线的反射峰波长随着悬浮泥沙浓度的增加向着较长波长方向移动,出现“红移现象”。研究提出的基于反射峰处的 HJ CCD 第 4 和第 3 波段等效反射率比值作为遥感因子,与悬浮泥沙浓度之间有很强的相关性,决定系数在 0.9 以上,建立了基于此波段比值遥感因子的指数模型。反演结果表明该模型能较好地描述杭州湾悬浮泥沙的空间分布,证明国产 HJ CCD 卫星影像数据可以用于中国近海水色的遥感研究。研究结果可以补充杭州湾本地水体光谱研究的不足,也可以为今后建立区域化遥感反演模式提供参考,同时对中、小尺度水体的水质监测以及后续星座的发展具有重要的理论和现实意义。

志 谢 此次野外实验数据的获取得到了杭州师范大学遥感与地球科学研究院的窦文洁、李凡、袁小红和周方方的鼎力协助,同时 HJ CCD 影像数据以及相关参数的获取得到了资源卫星应用中心相关部门的大力支持,在此表示衷心地感谢!

参考文献(References)

陈鸣,李士鸿,刘小靖. 1991. 长江口悬浮泥沙遥感信息处理和分析. 水利学报,5(5):47-51

Chen S S, Fang L G, Zhang L X and Huang W R. 2009. Remote sensing of turbidity in seawater intrusion reaches of Pearl River Estuary - a case study in Modaomen water way, China. Estuarine, Coastal and Shelf Science, 82(1): 119-127 [DOI: 10.1016/j.ecss.2009.01.003]

Chen S S, Huang W R, Chen W Q and Wang H Q. 2011. Remote sensing analysis of rainstorm effects on sediment concentrations in Apalachicola Bay, USA. Ecological Informatics, 6(2): 147-155 [DOI: 10.1016/j.ecoinf.2010.12.001]

Chen X L, Li Y S, Liu Z G, Yin K D, Li Z L, Wai O W H and King B. 2004. Integration of multi-source data for water quality classification in the Pearl River estuary and its adjacent coastal waters of Hong Kong. Continental Shelf Research, 24(16): 1827-1843 [DOI: 10.1016/j.csr.2004.06.010]

程天文,赵楚年. 1985. 我国主要河流入海径流量、输沙量及对沿岸的影响. 海洋学报,7(4):460-471

Doxaran D, Froidefond J M, Lavender S and Castaing P. 2002. Spectral signature of highly turbid waters-Application with SPOT data to quantify suspended particulate matter concentrations. Remote Sensing of Environment, 81(1): 149-161 [DOI: 10.1016/S0034-4257(01)00341-8]

Gin K Y H, Koh S T and Lin L L. 2003. Spectral irradiance profiles of suspended marine clay for the estimation of suspended sediment concentration in tropical waters. International Journal of Remote Sensing, 24(16): 3235-3245 [DOI: 10.1080/01431160110114934]

韩震,恽才兴,蒋雪中. 2003. 悬浮泥沙反射光谱特性实验研究. 水利学报,(12):118-122

何青,恽才兴,时伟荣. 1999. 长江口表层水体悬沙浓度场遥感分析. 自然科学进展,9(2):160-164

Hu C M, Chen Z Q, Clayton T D, Swarzenski P, Brock J C and Muller-Karger F E. 2004. Assessment of estuarine water-quality indicators using MODIS medium-resolution bands: Initial results from Tampa Bay, FL. Remote Sensing of Environment, 93(3): 423-441 [DOI: 10.1016/j.rse.2004.08.007]

Hui F M, Xu B, Huang H B, Yu Q and Gong P. 2008. Modeling spatial-temporal change of Poyang Lake using multitemporal Landsat imagery. International Journal of Remote Sensing, 29(20): 5767-5784 [DOI: 10.1080/01431160802060912]

李传荣,贾媛媛,胡坚,李子扬. 2008. HJ-1 光学卫星遥感应用前景分析. 国土资源遥感,(3):1-3,9

李京. 1987. 利用 NOAA 卫星的 AVHRR 数据监测杭州湾海域的悬浮泥沙含量. 海洋学报,9(1):132-135

李四海. 2001. 近海海洋水以遥感机理及其应用. 上海: 华东师范大学

刘志国,周云轩,蒋雪中,沈芳. 2006. 近岸Ⅱ类水体表层悬浮泥沙浓度遥感模式研究进展. 地球物理学进展,21(1):321-326

Morel A and Prieur L. 1977. Analysis of variations in ocean color. Limnology and Oceanography, 22(4): 709-722 [DOI: 10.4319/lo.1977.22.4.0709]

Mueller J L and Austin R W. 1995. Ocean Optics Protocols for SeaWiFS Validation (NASA Technical Memo 104566) vol 25 (Greenbelt, MD: NASA GSFC) p 24

唐军武,田国良,汪小勇,王晓梅,宋庆君. 2004. 水体光谱测量与分析 I: 水面以上测量法. 遥感学报,8(1):37-44

Tassan S. 1997. A numerical model for the detection of sediment concentration in stratified river plumes using Thematic Mapper data. International Journal of Remote Sensing, 18(12): 2699-2705 [DOI: 10.1080/014311697217567]

王繁,周斌,徐建明,凌在盈,周根娣. 2009. 杭州湾混浊水体表面光谱测量及光谱特征分析. 光谱学与光谱分析,29(3):730-734

Wang M H and Shi W. 2007. The NIR-SWIR combined atmospheric correction approach for MODIS ocean color data processing. Optics Express, 15(24): 15722-15733 [DOI: 10.1364/OE.15.015722]

Wang M H, Shi W and Tang J W. 2011. Water property monitoring and assessment for China's inland Lake Taihu from MODIS-Aqua measurements. Remote Sensing of Environment, 115(3): 841-854 [DOI: 10.1016/j.rse.2010.11.012]

Wu G F, De Leeuw J, Skidmore A K, Prins H H T and Liu Y L. 2008. Comparison of MODIS and Landsat TM5 images for mapping tempo-spatial dynamics of Secchi disk depths in Poyang Lake national nature reserve, China. International Journal of Remote Sensing, 29(8): 2183-2198 [DOI: 10.1080/01431160701422254]

吴华林,沈焕庭,严以新,王永红. 2006. 长江口入海泥沙通量初步研究. 泥沙研究,(6):75-81